Check for updates

High carbon utilization in CO_2 reduction to multi-carbon products in acidic media

Yi Xie [1,7], Pengfei Ou [2,7], Xue Wang [2,7], Zhanyou Xu [1], Yuguang C. Li [3], Ziyun Wang [4], Jianan Erick Huang[2], Joshua Wicks [2], Christopher McCallum [5], Ning Wang[2], Yuhang Wang [2], Tianxiang Chen[6], Benedict T. W. Lo[6], David Sinton [5], Jimmy C. Yu [1], Ying Wang [1] ✉ and Edward H. Sargent [2] ✉

Renewable electricity-powered CO_2 reduction to multi-carbon (C_{2+}) products offers a promising route to realization of low-carbon-footprint fuels and chemicals. However, a major fraction of input CO_2 (>85%) is consumed by the electrolyte through reactions with hydroxide to form carbonate/bicarbonate in both alkaline and neutral reactors. Acidic conditions offer a solution to overcoming this limitation, but also promote the hydrogen evolution reaction. Here we report a design strategy that suppresses hydrogen evolution reaction activity by maximizing the co-adsorption of CO and CO_2 on Cu-based catalysts to weaken H* binding. Using density functional theory studies, we found Pd–Cu promising for selective C_{2+} production over C_1, with the lowest ΔG_{OCCOH*} and ΔG_{OCCOH*} - ΔG_{CHO*}. We synthesized Pd–Cu catalysts and report a crossover-free system (liquid product crossover <0.05%) with a Faradaic efficiency of $89 \pm 4\%$ for CO_2 to C_{2+} at 500 mA cm^{-2}, simultaneous with single-pass CO_2 utilization of $60 \pm 2\%$ to C_{2+}.

Multi-carbon (C_{2+}) products derived from renewable electricity-powered CO_2 electroreduction (CO_2RR), such as with ethylene, ethanol and propanol, are of interest due to their high market value and the present-day energy density associated with their production[1–11]. Previous literature has focused therefore on the development of efficient catalysts and reactors for selective CO_2 to C_{2+} (refs. [11–14]). In these reactors, alkaline or neutral pH electrolytes are typically employed to suppress the competing hydrogen evolution reaction (HER) while promoting C–C coupling on the heterogeneous electrocatalyst[15].

Reliance, in regard to CO_2RR, on alkaline and neutral electrolytes leads to carbonate formation[15–18]. During both CO_2RR and HER, the consumption of H$^+$ creates a locally alkaline environment near the catalyst surface. One CO_2 molecule then reacts with two OH$^-$ to produce one equivalent of CO_3^{2-} for every two electrons transferred[16,19]. This militates against high CO_2 utilization efficiency—the percentage of CO_2 converted per total CO_2 input[17]. Furthermore, transport of carbonate to the anode and consequent evolution of CO_2 mandates costly separation and recovery of CO_2 from the anode stream. This effect is even more pronounced for multi-electron transfer products[16]. When C_{2+} chemicals are pursued, at least 75% of input CO_2 is consumed to form carbonate rather than being reduced, representing a major obstacle on the path to cost-effective CO_2 electrolysis[16,19,20].

Liquid product crossover also requires addressing: formate, acetate and ethanol move through the anion exchange membrane (AEM) by migration, diffusion and electro-osmotic drag, leading to product loss[21–24]. This effect becomes more evident with increased operating current density—typically 30% of liquid products are lost at 200 mA cm^{-2} when employing known AEMs[25].

The operation of CO_2RR under acidic conditions addresses the challenges of previous neutral and alkaline electrolyte systems. A high proton concentration in the electrolyte and the use of Nafion membrane as the separator are expected to minimize carbonate formation and liquid product crossover[18,26,27]. However, CO_2RR does not normally proceed efficiently in acidic electrolyte, especially when multi-carbon products are intended, the result of kinetically favoured HER under these conditions. H*, an intermediate for HER, competes with the adsorption of CO* over active sites during CO_2RR[28].

We reasoned that weakening the binding energy of H* while increasing CO* coverage could potentially suppress HER while enhancing C–C coupling for CO_2 (refs. [28,29]). Here we report catalysts exhibiting increased efficiency under acidic CO_2RR. We introduce bimetallic X–Cu catalysts that modulate local CO* coverage and suppress H* adsorption through adsorbate–adsorbate interactions[28,29]. Using density functional theory (DFT) calculations, we first screened different metals with a strong affinity towards CO* and found Pd–Cu to be the most promising candidate for CO_2 to C_{2+} in acid, because it exhibits the lowest ΔG_{OCCOH*} and, simultaneously, the lowest $\Delta G_{OCCOH*} - \Delta G_{CHO*}$, which, taken together, suggest high activity and selectivity to C_{2+} products. Experimentally, we synthesized Pd–Cu bimetallic catalysts for implementation in an acidic CO_2RR electrolyser employing an acidic bulk environment and operating under conditions that produce a mildly alkaline local environment at the catalyst surface. This pH gradient ensures that carbonate locally generated is converted back to CO_2 to enhance carbon utilization and promote surface C–C coupling for C_{2+} production. We then demonstrate liquid product crossover <0.05% with a CO_2-to-C_{2+} Faradaic efficiency (FE) of $89 \pm 4\%$, and

[1]Department of Chemistry, The Chinese University of Hong Kong, Hong Kong, China. [2]Department of Electrical and Computer Engineering, University of Toronto, Toronto, Ontario, Canada. [3]Department of Chemistry, University at Buffalo, State University of New York, Buffalo, New York, USA. [4]School of Chemical Sciences, The University of Auckland, Auckland, New Zealand. [5]Department of Mechanical and Industrial Engineering, University of Toronto, Toronto, Ontario, Canada. [6]Department of Applied Biology and Chemical Technology, The Hong Kong Polytechnic University, Hong Kong, China. [7]These authors contributed equally: Yi Xie, Pengfei Ou, Xue Wang. ✉e-mail: ying.b.wang@cuhk.edu.hk; ted.sargent@utoronto.ca
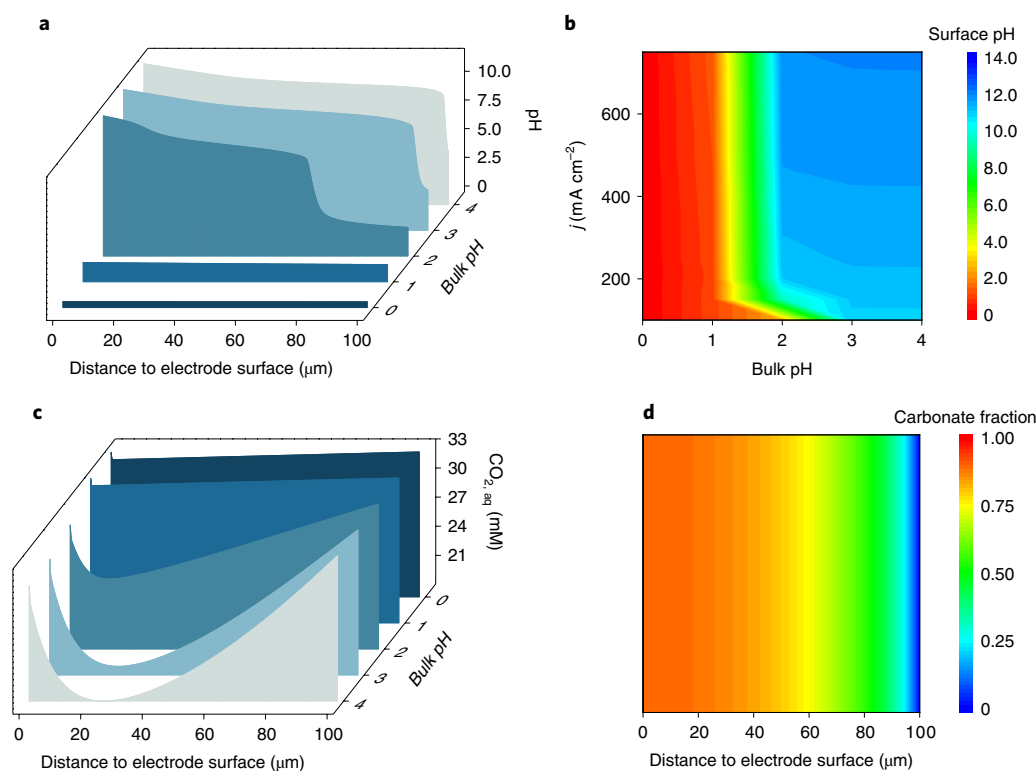
Fig. 1 | Profile of local species (CO_2 and H^+). a,b, Modelled pH changes along the catalyst surface in solution at different pH values under an applied current density of 500 mA cm^{-2} (**a**) and surface pH at varying applied current density (j) and bulk pH (**b**). **c,d**, Concentration profile of CO_2 under different solution pH values (**c**) and carbonate fraction in solution at pH 2.0 under an applied current density of 500 mA cm^{-2} (**d**). The carbonate fraction is calculated by the ratio between carbonate (CO_3^{2-})/bicarbonate (HCO_3^-) and the sum of carbon species (HCO_3^-, CO_3^{2-}, $CO_{2,aq}$). $CO_{2,aq}$ is the concentration of dissolved CO_2.

single-pass carbon efficiency of $60 \pm 2\%$ to C$_{2+}$ (total CO_2 utilization of $68 \pm 4\%$ when considering the sum of C$_1$ and C$_{2+}$ products) at 500 mA cm^{-2} in acidic media.

Results

Local species concentration profile. To address kinetically favoured HER in acidic media, we first sought a suitable reaction environment for CO_2RR by balancing bulk solution pH and carbonate formation. The Bjerrum plot of the carbonate system shows that CO_2 will be the dominant species at pH ≤ 4.0, suggesting a range of pH window options for acidic CO_2RR[30]. We used finite-element simulations to model the local environment of CO_2RR in an acidic electrolyser, adopting a previously reported one-dimensional (1D) domain diffusion-reaction model (Supplementary Note 1)[13,31,32].

We first screened interfacial pH changes under varying solution pH at current density 500 mA cm^{-2} (ref. [32]). No obvious pH change was observed from the electrode surface to the bulk solution at pH 0—the result of excess H^+ (Fig. 1a). For solutions with pH >2.0, a pH gradient, resulting from limited mass transport of protons under high current density, was formed at the diffusion layer, in agreement with experimental observations[27].

We also note the dependence of surface pH on applied current density at varying bulk pH (Fig. 1b and Supplementary Fig. 3). When we work with electrolytes at pH ≥ 2.0, depletion of H^+ becomes more evident with increasing current density, the result of limited availability of local H^+ to support the high reaction rate of the proton-coupled electron transfer reactions CO_2RR and HER (Fig. 1b). For solution at pH 2.0 with current density >150 mA cm^{-2}, surface pH increases to mildly alkaline (>9.5), leading to depletion of $CO_{2,aq}$ and the formation of carbonate (Fig. 1b,c).

The concentration of carbonate rapidly decreases and carbonate is converted back to CO_2 in the diffusion layer, the result of lower pH within the bulk electrolyte (Fig. 1a,d). The local CO_2 fraction rises from 0.12 to 1.0, indicating no CO_2 loss to carbonate formation during CO_2RR for bulk pH 2.0 electrolyte. Under conditions of pH 3.0 and 4.0, it is noted that CO_2 is depleted almost completely (Supplementary Fig. 4). We thus turned our focus to bulk pH 2.0 solutions to balance available local CO_2 with bulk acidity for current densities >150 mA cm^{-2}.

Design of catalysts for acidic CO_2RR. Previous work indicated that metals with a strong binding affinity towards CO* show a weakening of H* binding affinity, the result of adsorbate–adsorbate interactions[28,29]. We screened different bimetallic X–Cu (X = Cr, Mo, W, Mn, Re, Fe, Ru, Co, Rh, Ir, Ni, Pt and Pd), with X having a strong affinity towards CO* (refs. [28,29]). We considered CH$_4$ and C$_2$H$_4$ as representative examples for C$_1$ and C$_{2+}$ products, respectively. For C$_1$ products, the CHO pathway is selected since proton–electron transfer to CO* via the CHO pathway is lower than that of the COH pathway[33], and further protonation can take place via CH$_2$O* and OCH$_3$* to CH$_4$ (Supplementary Figs. 10 and 11). For C$_{2+}$ production we chose the OCCOH pathway—CO* dimerization to OCCO* and subsequent protonation to OCCOH*—followed by the formation of CCO*, CHCO* and C$_2$H$_4$ (ref. [34]) (Supplementary Figs. 10 and 11). With DFT, we first calculated Gibbs free energies for the formation of CHO* (ΔG_{CHO*}) and OCCOH* (ΔG_{OCCOH*}) on the (111) surface of bimetallic X–Cu. We chose ΔG_{OCCOH*} as an indicator of the propensity of C$_{2+}$ product generation, and $\Delta G_{OCCOH*} - \Delta G_{CHO*}$ for the selectivity of CO_2RR to C$_{2+}$ versus C$_1$ products. We observed a scaling relation between ΔG_{OCCOH*} and $\Delta G_{OCCOH*} - \Delta G_{CHO*}$ (Fig. 2a):
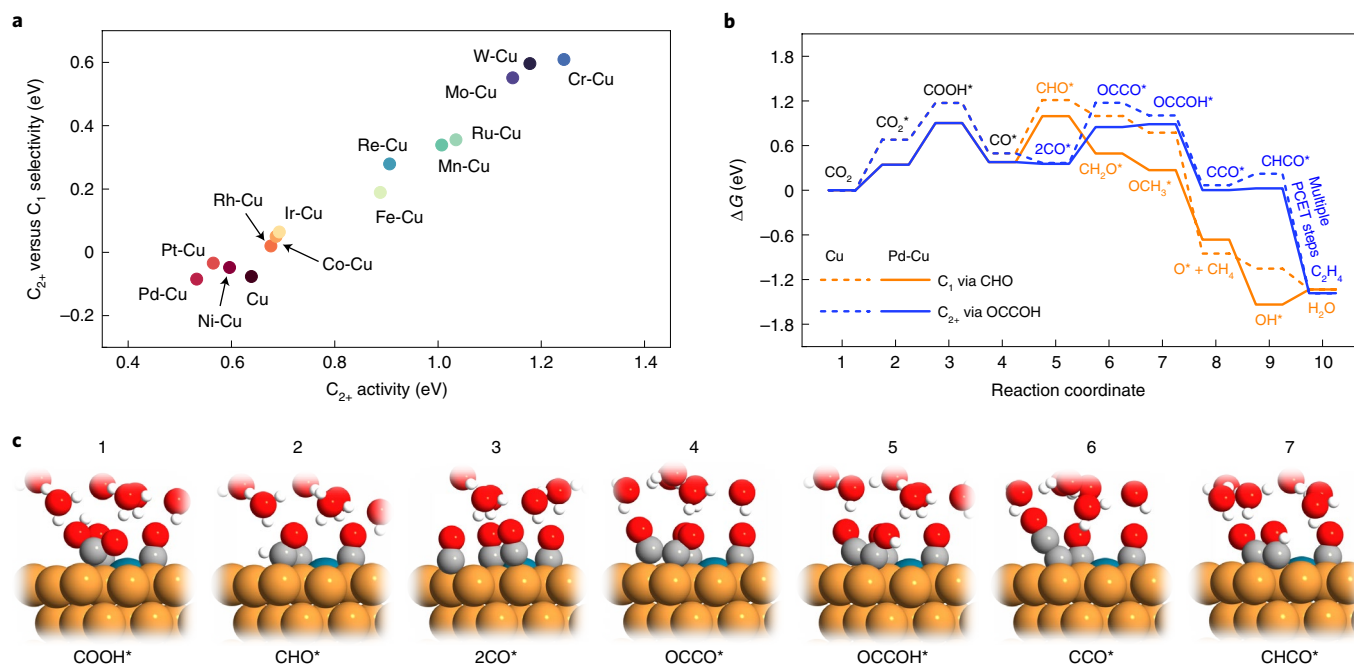
Fig. 2 | DFT calculation of CO_2RR on bimetallic X–Cu(111). a, Two-dimensional C_{2+} activity (ΔG_{OCCOH^*}) and C_{2+} versus C_1 selectivity ($\Delta G_{OCCOH^*} - \Delta G_{CHO^*}$) plot of CO_2RR to C_1 and C_{2+} products. **b,** Free energy diagram of CO_2RR via the CHO pathway toward C_1 products (orange), where CH_4 is used as the representative product, and the OCCOH pathway toward C_{2+} products (blue), where C_2H_4 is utilized as the representative product. Solid and dashed lines represent Pd–Cu and Cu, respectively. **c,** Geometries of selected reaction intermediates involved in different pathways in generation of both C_1 and C_{2+} products (green, palladium; orange, copper; red, oxygen; grey, carbon; white, hydrogen).

Pd–Cu was found to be the most promising candidate for active and selective C_{2+} production, with the lowest values of ΔG_{OCCOH^*} and $\Delta G_{OCCOH^*} - \Delta G_{CHO^*}$ (Methods).

We carried out further DFT studies on Cu and Pd–Cu to investigate the reaction pathway of CO_2RR to C_1 and C_{2+} products. As shown in Fig. 2b,c, an increase in CO* coverage on Pd–Cu facilitated CO_2RR due to stronger adsorption of CO_2—that is, 0.68 eV on Cu versus 0.34 eV on Pd–Cu. This also led to less efficient CO* desorption and a greater likelihood of CO* protonation, or of coupling to further-reduced products on Pd–Cu, since CO* is a key reaction intermediate in CO_2RR in branching to C_1 versus C_{2+} products. On both Cu and Pd–Cu (Fig. 2b), the potential-determining step for C_1 production is the protonation of CO* to CHO* while the generation of C_{2+} products is limited by CO* dimerization. Compared with Cu, enhanced C_{2+} versus C_1 activity/selectivity is observed on Pd–Cu due to reduced ΔG_{OCCOH^*} and $\Delta G_{OCCOH^*} - \Delta G_{CHO^*}$.

The selectivity of CO_2RR toward C_{2+} products can be improved further via HER suppression[28,35]: Pd–Cu strongly adsorbs CO_2RR reaction intermediates, covers the catalyst surface and decreases the availability of vacant active sites for HER. The adsorption energy of H* is 0.2 eV weaker on Pd–Cu compared to that on Cu, suggesting suppressed HER. We also note that future, in-depth studies of kinetics involving water and charge transfer will contribute to revealing the origins of selectivity for CO_2R versus HER in aqueous solution, enabling further advances in catalyst design[36,37].

Electrochemical CO_2RR in acidic solution. In light of 1D transport simulations and DFT calculations, we sought to prepare Pd–Cu catalysts and evaluate their CO_2RR activity in the electrolyte at pH ~2.0. Pd was introduced onto a Cu/polytetrafluoroethylene (PTFE) catalyst through a galvanic exchange reaction enabled by the difference in potential of these two metals[38,39]. First we prepared, via sputter deposition, a 400-nm-thick layer of Cu catalysts on the surface of PTFE nanofibres. We then immersed the Cu/PTFE in a

N_2-saturated $PdCl_2$ aqueous solution to prepare the Pd–Cu catalysts on PTFE (Fig. 3a,b and Supplementary Fig. 13) using galvanic replacement between Cu and $PdCl_2$, an approach that allows tuning of the ratio of Pd to Cu. Cu and Pd are uniformly distributed on the PTFE nanofibres in bright-field scanning transmission electron microscopy and energy-dispersive X-ray (EDX) elemental mapping (Fig. 3c). Pd $3d_{3/2}$ and Pd $3d_{5/2}$ with binding energy at 340.8 and 335.4 eV, respectively, were observed on X-ray photoelectron spectroscopy (XPS), showing the introduction of Pd (Fig. 3d)[40]. We prepared a series of Pd–Cu catalysts on PTFE with different Pd ratios (denoted by X% Pd–Cu, X = 4.6, 5.5, 6.2, 6.7, 7.2) for CO_2RR measurements (Fig. 3d,e).

CO_2RR performance was evaluated in a flow-cell reactor employing a three-electrode configuration and using 0.5 M K_2SO_4 (pH adjusted to 2.0 with sulfuric acid) aqueous solution as electrolyte. Figure 4a shows the FE of C_{2+} and H_2 with different levels of Pd at a current density of 250 mA cm⁻². We observed volcano behaviour correlating the selectivity of C_{2+} products to Pd concentration and an inverse trend for H_2 and C_1 FE values, with optimal results found at Pd 6.2%. A peak C_{2+} FE of 80% was observed for 6.2% Pd, while 68% was measured for bare Cu. When we further increased Pd concentration to >6.2%, FE for CO_2RR decreased with increased HER. The electrochemical capacitance measured on 6.2% Pd–Cu was 14% lower than on Cu/PTFE, while 6.2% Pd–Cu showed a 20% increase in partial current density to C_{2+}, notably higher than the relative difference in electrochemical surface area (Supplementary Figs. 16 and 17 and Supplementary Table 4).

We then carried out in situ Raman spectroscopy to investigate interactions between CO* and the catalytic surface to gain mechanistic insight into C–C coupling during CO_2RR on Pd–Cu and Cu (Supplementary Fig. 18). We observed a band associated with the atop-bound CO (>2,000 cm⁻¹) associated with C–C coupling[3,41], and observed it to be more pronounced for Pd–Cu compared with Cu. Compared with Cu, the blueshift of the Cu-CO stretch
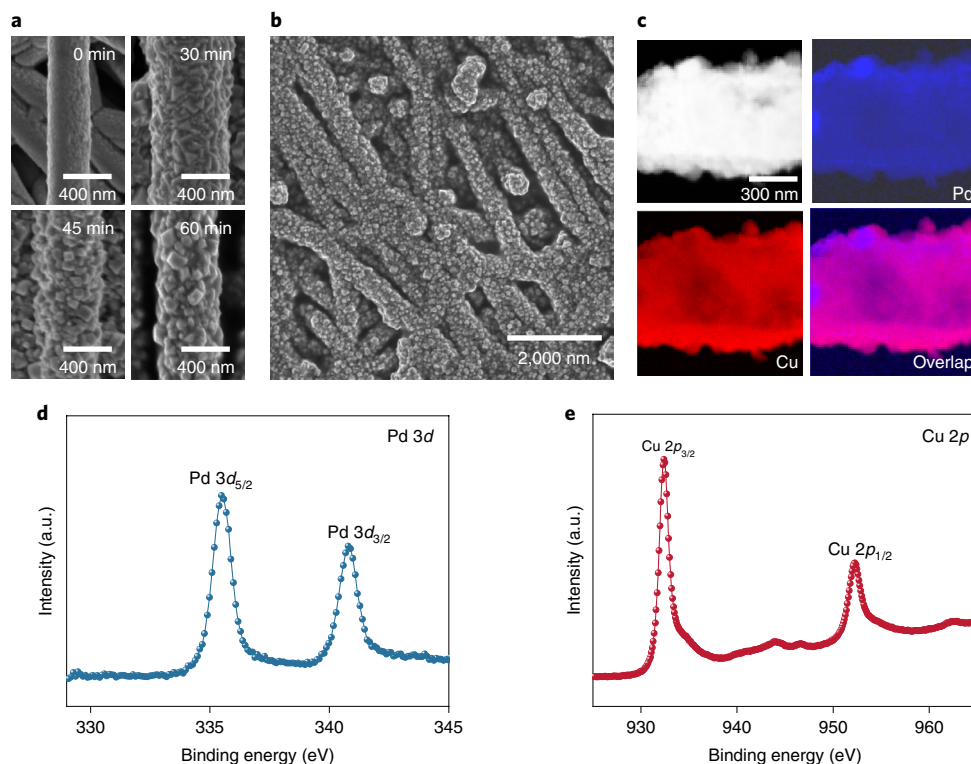
Fig. 3 | Structural and compositional characterization of Pd–Cu catalysts on PTFE. a, SEM image of a series of Pd–Cu catalysts with varying galvanic replacement reaction time. **b**, Low-magnification SEM for 6.2% Pd–Cu catalysts on PTFE. **c**, TEM image (upper left) of Pd–Cu catalyst and corresponding EDX mapping of Cu and Pd. **d,e**, High-resolution XPS spectra of Pd 3d (**d**) and Cu 2p (**e**) for 6.2% Pd–Cu catalysts on PTFE. au, Arbitrary units.

band—in the range 375–425 cm^{-1}—was evident on Pd–Cu, suggesting a stronger Cu-CO bond on Pd–Cu, also beneficial to C–C coupling[8].

The product distribution of CO$_2$RR on 6.2% Pd–Cu in the current density range (100–750 mA cm^{-2}) is shown in Fig. 4b. HER selectivity was as high as 16% at 100 mA cm^{-2}, consistent with finite-element modelling that showed a higher local proton concentration. When we increased current density a mildly locally alkaline environment emerged, as suggested in Fig. 1a,b, since local protons are consumed rapidly. Beginning at 200 mA cm^{-2} and above, experimental FE$_{H2}$ and FE$_{C1}$ begin to decrease and total FE$_{C2+}$ increased. At 500 mA cm^{-2} we achieved the highest FE for C$_{2+}$ products of 87%, with a partial current density to C$_{2+}$ equal to 440 mA cm^{-2} (Fig. 4b,c). We compared this selectivity of CO$_2$ to C$_{2+}$ in acidic solution with previous reports (Fig. 4g and Supplementary Table 5)[18,24,42–44]. The devices maintained stable operation for 4.5 h at 500 mA cm^{-2}, with FE$_{C2+}$ >70% (Fig. 4d). The slight decline in current density may have arisen from wetting of the gas-diffusion layer[45–50]. No appreciable structure changes were observed on Pd–Cu/PTFE electrodes after the reaction (Supplementary Figs. 19–21).

Acidic media minimize carbonate formation, and thus should contribute to overcoming carbon utilization limits witnessed in neutral and alkaline solutions. By progressively reducing the flow rate of CO$_2$ from 50 to 2 standard cc min^{-1} (sccm), we achieved single-pass carbon efficiency (SPCE) of 68% for the totality of CO$_2$RR products: 60% of CO$_2$ introduced at the inlet was converted to C$_{2+}$ at the outlet (at 2 sccm and 500 mA cm^{-2}; Fig. 4e). We compare this SPCE with previous CO$_2$-to-C$_{2+}$ reports in Fig. 4f and Supplementary Table 6.

We further examined liquid product crossover in the present system with that seen in an AEM electrolyser. As shown in Fig. 4g, crossover of liquid products was observed within 0.5 h in an AEM electrolyser—5.4, 39 and 1.0% for formate, acetate and

ethanol, respectively, while in a Nafion-based CO$_2$ electrolyser we were unable to detect liquid products in the anolyte with no evidence of ethanol, acetate or formate in the anolyte following 4.5 h of electrolysis.

Conclusions

We report herein crossover-free, high-single-pass carbon-utilization CO$_2$-to-C$_{2+}$ electrosynthesis. Finite-element studies show that pH 2.0 was the most suitable reaction condition for acidic CO$_2$RR, a judicious balance between bulk pH and carbonate formation. DFT results show that the introduction of Pd to Cu enhanced local CO* coverage to promote C–C coupling. The high affinity for CO* competes with the active site of H* to weaken H-binding energy, suppressing the HER and thus enabling high selectivity to C$_{2+}$ on Pd–Cu. Experimentally we synthesized a series of Pd–Cu catalysts for CO$_2$RR under acidic conditions and report a single-pass carbon efficiency for CO$_2$ to C$_{2+}$ of 60% at 500 mA cm^{-2}. These findings suggest future directions toward further progress in overcoming CO$_2$ loss in CO$_2$ electrolysers.

Methods

Profile modelling of local species. Concentration profiles of local species (CO$_2$, HCO$_3^-$, CO$_3^{2-}$, OH$^-$, H$^+$) were simulated as a reaction-diffusion model by COMSOL (COMSOL Multiphysics v.5.6), a model based on previous reports[14,30,31]. The geometry was defined in 1D based on an experimental set-up (Supplementary Fig. 1), including a 400-nm-thick cathode catalyst layer and an electrolyte domain located adjacent to the cathode (0–100 μm) to represent the diffusion layer[51]. The model included acid–base carbonate equilibria, CO$_2$ reduction reaction and dilute species transport physics in liquid phase. A time-dependent study was adapted to simulate species evolution toward steady state (Supplementary Note 1).

DFT calculations. Electronic structure calculations were carried out with the Perdew–Burke–Ernzerhof exchange-correlation[52] functional in a plane
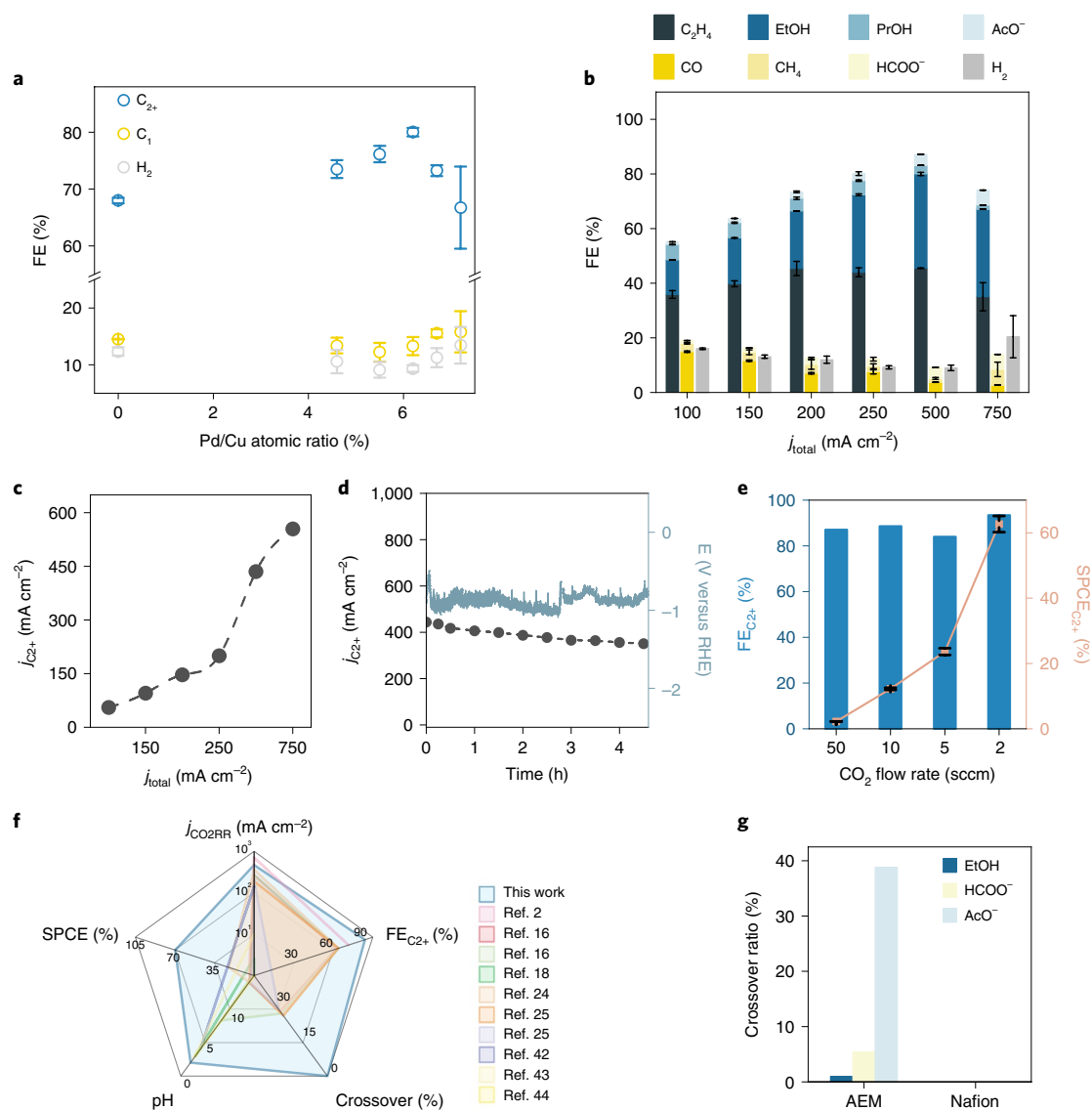
Fig. 4 | CO₂RR performance of Pd–Cu catalysts. a, FE of C_{2+} products (ethanol, n-propanol, acetate and ethylene), C_1 (methane, carbon monoxide and formate) and H_2 on a series of Pd–Cu catalysts on PTFE with increasing atomic percentage of Pd. **b,c**, FE values of all products (**b**) and C_{2+} partial current density (**c**) on 6.2% Pd–Cu catalysts under different applied current densities. Flow rate of the CO_2 inlet was 50 sccm. **d**, CO_2RR stability measurement of C_{2+} products during 4.5 h of electrolysis with an applied current density of 500 mA cm⁻². **e**, FE values and $SPCE_{C2+}$ of CO_2 to C_{2+} on 6.2% Pd–Cu at different CO_2 flow rates (applied current density, 500 mA cm⁻²). **f**, Comparison of CO_2RR partial current density, C_{2+} product FE, liquid product crossover fraction, pH of bulk electrolyte and SPCE of 6.2% Pd–Cu with state-of-art CO_2RR catalysts. Comparison limited to reports with pH ≤4.0 or with total current density >10 mA cm⁻². **g**, Product crossover for Pd–Cu catalyst in an AEM CO_2 electrolyser after 0.5 h of operation, and in a Nafion CO_2 electrolyser after 4.5 h. Values are means; **a,b,e**, error bars indicate s.d. ($n = 3$ replicates).

wave pseudo-potential implementation using the Vienna ab initio simulation package[53,54]. Plane-wave cut-off energy of 450 eV and $3 \times 3 \times 1$ Γ-centred k-point sampling, generated by the Monkhorst–Pack scheme, were used for all calculations[55]. A hexagonal charged water overlayer—that is, five water molecules and one hydronium (H_3O^+)—was included to take into consideration of both field and solvation effects[56]. The zero-damping DFT-D3 method of Grimme et al. was also considered for a better description of long-range van der Waals interactions[57]. All atoms in the two bottom-most layers were fixed during structural optimization while other atoms, together with the adsorbates, were allowed to relax. Geometries were optimized by considering different adsorption sites on the surfaces with respect to the charged water overlayer, and those with the lowest energy from DFT calculations are reported. Ab initio molecular dynamics (AIMD) simulations were conducted in a constant-volume, constant-temperature ensemble and performed for 10 ps with the time step set to 0.5 fs, to optimize the structure of the charged water overlayer. The Nosé–Hoover thermostat method was used to maintain the temperature at 300 K. Reaction intermediates in CO_2R and HER were included in the optimized geometry from AIMD simulations, and again to perform DFT calculations.

Calculations were performed on the (111) surface of face-centred cubic Cu using a $3 \times 3 \times 4$ periodic cell with a vacuum layer of thickness 12 Å, since the (111) surface is generally found to have minimum surface energy. Bimetallic X–Cu (X = Cr, Mo, W, Mn, Re, Fe, Ru, Co, Rh, Ir, Ni and Pd) was constructed when one of the Cu atoms on the surface was substituted by an X atom. We found that X_1Cu_2 hollow sites preferentially favoured CO adsorption and increased CO* surface coverage, which led to further 2CO* adsorption besides the active sites compared with Cu. This structure was determined by assuming that C_1 and C_{2+} products were produced only on Cu sites, with the adsorbed 2CO* around the X atom near these active sites not participating in those reactions generating C_1 and C_{2+} products.

Contributions to Gibbs free energies for each non-adsorbed species and adsorbates are summarized in Supplementary Table 9. Zero-point energies, entropies and heat capacities were calculated from harmonic oscillator approximation, and used to convert electronic energies directly determined from DFT calculations into Gibbs free energies at 298.15 K when applying the computational hydrogen electrode model[58]. We note that the Gibbs free energies determined from our calculations for different bimetallic X–Cu systems provide a reasonable prediction of semiquantitative thermodynamic trends under

electrochemical conditions, since we ignore the presence of transition states and charged intermediates on surfaces[59]. It is more appropriate for electrochemistry if grand canonical DFT calculations are performed as implemented in the software programme JDFTx[60,61], where all intermediates are treated at the same potential.

Electrode preparation. All chemicals were used without further purification. The Cu/PTFE electrode was prepared using a magnetron sputtering system (Denton Explorer 14 Sputtering System). Cu catalysts (Cu target, 99.99%, Kurt J. Lesker Co.) with a thickness of 400 nm were sputtered on PTFE membranes (pore size 450 nm, Beijing Zhongxingweiye Instrument Co.) at a sputtering rate of $0.778\,Å\,s^{-1}$. Using galvanic replacement, we introduced Pd to the Cu/PTFE substrate. The Cu/PTFE electrodes were immersed in an aqueous solution of $PdCl_2$ (99.999% metal basis, Aladdin) at a concentration of $5\,mmol\,l^{-1}$ at room temperature. Catalysts with different Pd/Cu ratios were synthesized by controlling reaction time. An Ag/AgCl electrode (saturated with KCl, IDA) and Pt mesh ($30 \times 15\,mm^2$, 99.99%, Gaoss Union) were used as reference and counter electrode, respectively.

Characterization. To characterize catalyst morphology, scanning electron microscopy (SEM) images were collected using TESCAN MAIA3. Transmission electron microscopy (TEM) and corresponding EDX elemental mapping were collected using Tecnai F20 microscope. X-ray diffraction patterns were recorded on Rigaku SmartLab with Mo radiation. The surface composition of electrodes was characterized using a Nexsa XPS system using a 12 kV aluminium source.

Electrochemical measurements. Electrochemical measurements were conducted in flow-cell set-up with three chambers (Supplementary Fig. 8). A PTFE-based gas-diffusion electrode was fixed between the gas and catholyte chambers. A proton exchange membrane (Nafion 117, Fuel Cell Store) was used to separate the anode and cathode chambers; 40 ml of CO_2-saturated $0.5\,M\,K_2SO_4$ aqueous solution was used as electrolyte, circulated through the cathode and anode chambers at a rate of $6\,ml\,min^{-1}$ by two peristaltic pumps. Pure CO_2 gas (99.99%, Air Products) was continuously supplied to the gas chamber at a flow rate of $50\,ml\,min^{-1}$. CO_2RR performance was tested using the chronopotentiometric method, with power supplied by an electrochemical workstation (ZAHNER ZENNIUM pro). Potentials versus the Ag/AgCl reference electrode were converted to the RHE reference scale using the following equation: $E_{RHE} = E_{Ag/AgCl} + 0.197V + 0.0591 \times pH$. Cell resistance was evaluated by performing electrochemical impedance spectroscopy measurement (CH Instruments, 660E).

Gaseous products were analysed using a gas chromatograph (Ramiin, GC 2060) equipped with flame ionization and thermal conductivity detectors. The calibration curves for CO, CH_4, C_2H_4 and H_2 were obtained using certified standard gas samples obtained from Scientific Gas Engineering Co. Liquid products were quantified using a nuclear magnetic resonance spectrometer (Bruker AVANCE III HD 500), with dimethyl sulfoxide as an internal standard.

FE for each product was calculated based on the following equation:

$$FE_i = \frac{z_i \times x_i \times F}{Q} \times 100 \tag{1}$$

where z_i is the number of electrons transferred for product, x_i is the number of moles of the product, F is Faraday's constant and Q is the total charge passed during electrolysis.

SPCE for C_{2+} products was calculated based on the following equation:

$$SPCE = \frac{60\,s \times \sum(I \times x_i \times FE_i \div (N_i \times F))}{flow\ rate(l/min) \times 1\,min \times 24.5(l/mol)} \tag{2}$$

where I is the applied current, FE_i is the FE of a specific group of products from CO_2 reduction, x_i is mole ratio of CO_2 to a specific product (for example, $x_i = 1$ for C_1 products while $x_i = 2$ for C_2 products) and N_i is the number of electron transfers for every specific product molecule.

Data availability
All data are available from the authors upon reasonable request.

References
1. De Luna, P. et al. What would it take for renewably powered electrosynthesis to displace petrochemical processes? *Science* **364**, eaav3506 (2019).
2. Dinh, C.-T. et al. CO_2 electroreduction to ethylene via hydroxide-mediated copper catalysis at an abrupt interface. *Science* **360**, 783–787 (2018).
3. Li, F. et al. Cooperative CO_2-to-ethanol conversion via enriched intermediates at molecule–metal catalyst interfaces. *Nat. Catal.* **3**, 75–82 (2020).
4. Li, J. et al. Constraining CO coverage on copper promotes high-efficiency ethylene electroproduction. *Nat. Catal.* **2**, 1124–1131 (2019).
5. Nitopi, S. et al. Progress and perspectives of electrochemical CO_2 reduction on copper in aqueous electrolyte. *Chem. Rev.* **119**, 7610–7672 (2019).
6. Ozden, A. et al. High-rate and efficient ethylene electrosynthesis using a catalyst/promoter/transport layer. *ACS Energy Lett.* **5**, 2811–2818 (2020).
7. Pang, Y. et al. Efficient electrocatalytic conversion of carbon monoxide to propanol using fragmented copper. *Nat. Catal.* **2**, 251–258 (2019).
8. Wang, X. et al. Efficient electrically powered CO_2-to-ethanol via suppression of deoxygenation. *Nat. Energy* **5**, 478–486 (2020).
9. Wang, X. et al. Efficient upgrading of CO to C_3 fuel using asymmetric C-C coupling active sites. *Nat. Commun.* **10**, 5186 (2019).
10. Verma, S., Lu, S. & Kenis, P. J. A. Co-electrolysis of CO_2 and glycerol as a pathway to carbon chemicals with improved technoeconomics due to low electricity consumption. *Nat. Energy* **4**, 466–474 (2019).
11. Luc, W. et al. Two-dimensional copper nanosheets for electrochemical reduction of carbon monoxide to acetate. *Nat. Catal.* **2**, 423–430 (2019).
12. Li, J. et al. Efficient electrocatalytic CO_2 reduction on a three-phase interface. *Nat. Catal.* **1**, 592–600 (2018).
13. de Arquer, F. P. G. et al. CO_2 electrolysis to multicarbon products at activities greater than 1 A cm^{-2}. *Science* **367**, 661–666 (2020).
14. Chen, X. et al. Electrochemical CO_2-to-ethylene conversion on polyamine-incorporated Cu electrodes. *Nat. Catal.* **4**, 20–27 (2020).
15. Chen, C., Li, Y. & Yang, P. Address the "alkalinity problem" in CO_2 electrolysis with catalyst design and translation. *Joule* **5**, 737–742 (2021).
16. Ma, M. et al. Insights into the carbon balance for CO_2 electroreduction on Cu using gas diffusion electrode reactor designs. *Energy Environ. Sci.* **13**, 977–985 (2020).
17. Rabinowitz, J. A. & Kanan, M. W. The future of low-temperature carbon dioxide electrolysis depends on solving one basic problem. *Nat. Commun.* **11**, 5231 (2020).
18. Bondue, C. J., Graf, M., Goyal, A. & Koper, M. T. M. Suppression of hydrogen evolution in acidic electrolytes by electrochemical CO_2 reduction. *J. Am. Chem. Soc.* **143**, 279–285 (2021).
19. Nabil, S. K., McCoy, S. & Kibria, M. G. Comparative life cycle assessment of electrochemical upgrading of CO_2 to fuels and feedstocks. *Green Chem.* **23**, 867–880 (2021).
20. Dinh, C.-T., Li, Y. C. & Sargent, E. H. Boosting the single-pass conversion for renewable chemical electrosynthesis. *Joule* **3**, 13–15 (2019).
21. Firouzjaie, H. A. & Mustain, W. E. Catalytic advantages, challenges, and priorities in alkaline membrane fuel cells. *ACS Catal.* **10**, 225–234 (2020).
22. Salvatore, D. A. et al. Designing anion exchange membranes for CO_2 electrolysers. *Nat. Energy* **6**, 339–348 (2021).
23. Li, Y. C. et al. Bipolar membranes inhibit product crossover in CO_2 electrolysis cells. *Adv. Sustain. Syst.* **2**, 1700187 (2018).
24. Ma, S. et al. One-step electrosynthesis of ethylene and ethanol from CO_2 in an alkaline electrolyzer. *J. Power Sources* **301**, 219–228 (2016).
25. Zhang, J., Luo, W. & Züttel, A. Crossover of liquid products from electrochemical CO_2 reduction through gas diffusion electrode and anion exchange membrane. *J. Catal.* **385**, 140–145 (2020).
26. Goyal, A., Marcandalli, G., Mints, V. A. & Koper, M. T. M. Competition between CO_2 reduction and hydrogen evolution on a gold electrode under well-defined mass transport conditions. *J. Am. Chem. Soc.* **142**, 4154–4161 (2020).
27. Ooka, H., Figueiredo, M. C. & Koper, M. T. M. Competition between hydrogen evolution and carbon dioxide reduction on copper electrodes in mildly acidic media. *Langmuir* **33**, 9307–9313 (2017).
28. Zhang, Y.-J., Sethuraman, V., Michalsky, R. & Peterson, A. A. Competition between CO_2 reduction and H_2 evolution on transition-metal electrocatalysts. *ACS Catal.* **4**, 3742–3748 (2014).
29. Cave, E. R. et al. Trends in the catalytic activity of hydrogen evolution during CO_2 electroreduction on transition metals. *ACS Catal.* **8**, 3035–3040 (2018).
30. Wolf-Gladrow, D. A., Zeebe, R. E., Klaas, C., Körtzinger, A. & Dickson, A. G. Total alkalinity: the explicit conservative expression and its application to biogeochemical processes. *Mar. Chem.* **106**, 287–300 (2007).
31. Weng, L. C., Bell, A. T. & Weber, A. Z. Modeling gas-diffusion electrodes for CO_2 reduction. *Phys. Chem. Chem. Phys.* **20**, 16973–16984 (2018).
32. Yin, Z. L. et al. An alkaline polymer electrolyte CO_2 electrolyzer operated with pure water. *Energy Environ. Sci.* **12**, 2455–2462 (2019).
33. Liu, X. et al. Understanding trends in electrochemical carbon dioxide reduction rates. *Nat. Commun.* **8**, 15438 (2017).
34. Peng, H. et al. The role of atomic carbon in directing electrochemical CO_2 reduction to multicarbon products. *Energy Environ. Sci.* **14**, 473–482 (2021).
35. Lamoureux, P. S., Singh, A. R. & Chan, K. pH effects on hydrogen evolution and oxidation over Pt(111): insights from first-principles. *ACS Catal.* **9**, 6194–6201 (2019).
36. Zhao, X. & Liu, Y. Unveiling the active structure of single nickel atom catalysis: critical roles of charge capacity and hydrogen bonding. *J. Am. Chem. Soc.* **142**, 5773–5777 (2020).
37. Zhao, X. & Liu, Y. Origin of selective production of hydrogen peroxide by electrochemical oxygen reduction. *J. Am. Chem. Soc.* **143**, 9423–9428 (2021).

38. Xia, X., Wang, Y., Ruditskiy, A. & Xia, Y. 25th Anniversary article: galvanic replacement: a simple and versatile route to hollow nanostructures with tunable and well-controlled properties. *Adv. Mater.* **25**, 6313–6333 (2013).

39. Zhang, H. et al. Controlling the morphology of rhodium nanocrystals by manipulating the growth kinetics with a syringe pump. *Nano Lett.* **11**, 898–903 (2011).

40. Chen, C. et al. Coupling N_2 and CO_2 in H_2O to synthesize urea under ambient conditions. *Nat. Chem.* **12**, 717–724 (2020).

41. Gunathunge, C. M. et al. Spectroscopic observation of reversible surface reconstruction of copper electrodes under CO_2 reduction. *J. Phys. Chem. C Nanomater. Interfaces* **121**, 12337–12344 (2017).

42. Whipple, D. T., Finke, E. C. & Kenis, P. J. A. Microfluidic reactor for the electrochemical reduction of carbon dioxide: the effect of pH. *Electrochem. Solid State Lett.* **13**, B109–B111 (2010).

43. Wang, Z., Hou, P., Wang, Y., Xiang, X. & Kang, P. Acidic electrochemical reduction of CO_2 using nickel nitride on multiwalled carbon nanotube as selective catalyst. *ACS Sustain. Chem. Eng.* **7**, 6106–6112 (2019).

44. Shen, J. et al. Electrocatalytic reduction of carbon dioxide to carbon monoxide and methane at an immobilized cobalt protoporphyrin. *Nat. Commun.* **6**, 8177 (2015).

45. Ma, W. et al. Electrocatalytic reduction of CO_2 to ethylene and ethanol through hydrogen-assisted C–C coupling over fluorine-modified copper. *Nat. Catal.* **3**, 478–487 (2020).

46. Pan, H. & Barile, C. J. Electrochemical CO_2 reduction to methane with remarkably high Faradaic efficiency in the presence of a proton permeable membrane. *Energy Environ. Sci.* **13**, 3567–3578 (2020).

47. Li, Y. et al. Promoting CO_2 methanation via ligand-stabilized metal oxide clusters as hydrogen-donating motifs. *Nat. Commun.* **11**, 6190 (2020).

48. Reyes, A. et al. Managing hydration at the cathode enables efficient CO_2 electrolysis at commercially relevant current densities. *ACS Energy Lett.* **5**, 1612–1618 (2020).

49. Yang, K., Kas, R., Smith, W. A. & Burdyny, T. Role of the carbon-based gas diffusion layer on flooding in a gas diffusion electrode cell for electrochemical CO_2 reduction. *ACS Energy Lett.* **6**, 33–40 (2021).

50. Lomax, D. J. et al. Ultra-low voltage electrowetting using graphite surfaces. *Soft Matter* **12**, 8798–8804 (2016).

51. Singh, M. R., Clark, E. L. & Bell, A. T. Effects of electrolyte, catalyst, and membrane composition and operating conditions on the performance of solar-driven electrochemical reduction of carbon dioxide. *Phys. Chem. Chem. Phys.* **17**, 18924–18936 (2015).

52. Perdew, J. P., Burke, K. & Ernzerhof, M. Generalized gradient approximation made simple. *Phys. Rev. Lett.* **77**, 3865–3868 (1996).

53. Kresse, G. & Hafner, J. Ab initio molecular dynamics for liquid metals. *Phys. Rev. B* **47**, 558–561 (1993).

54. Kresse, G. & Hafner, J. Ab initio molecular-dynamics simulation of the liquid-metal—amorphous-semiconductor transition in germanium. *Phys. Rev. B* **49**, 14251–14269 (1994).

55. Monkhorst, H. J. & Pack, J. D. Special points for Brillouin-zone integrations. *Phys. Rev. B* **13**, 5188–5192 (1976).

56. Montoya, J. H., Shi, C., Chan, K. & Nørskov, J. K. Theoretical insights into a CO dimerization mechanism in CO_2 electroreduction. *J. Phys. Chem. Lett.* **6**, 2032–2037 (2015).

57. Grimme, S., Antony, J., Ehrlich, S. & Krieg, H. A consistent and accurate ab initio parametrization of density functional dispersion correction (DFT-D) for the 94 elements H-Pu. *J. Chem. Phys.* **132**, 154104 (2010).

58. Nørskov, J. K. et al. Origin of the overpotential for oxygen reduction at a fuel-cell cathode. *J. Phys. Chem. B* **108**, 17886–17892 (2004).

59. Alfonso, D. R., Tafen, D. N. & Kauffmann, D. R. First-principles modeling in heterogeneous electrocatalysis. *Catalysts* **8**, 424 (2018).

60. Sundararaman, R. & Goddard, W. A. The charge-asymmetric nonlocally determined local-electric (CANDLE) solvation model. *J. Chem. Phys.* **142**, 064107 (2015).

61. Sundararaman, R. et al. JDFTx: software for joint density-functional theory. *SoftwareX* **6**, 278–284 (2017).

Author contributions

Ying Wang and E.H.S. designed and supervised the project. Y.X. carried out electrochemical measurements, part of the COMSOL simulations and analysed data. P.O. carried out DFT calculations and analysed data. X.W. performed in situ Raman analysis. C.M. contributed part of the COMSOL modelling. T.C. and T.B.L. performed XPS measurements. Ying Wang, P.O., X.W., Y.X., Z.X., J.E.H., Y.C.L., J.W. and Z.W. co-wrote the paper. All authors discussed the results and contributed to the preparation of the manuscript.

Competing interests

The authors declare no competing interests.

Additional information

Supplementary information The online version contains supplementary material available at https://doi.org/10.1038/s41929-022-00788-1.

Correspondence and requests for materials should be addressed to Ying Wang or Edward H. Sargent.

Peer review information *Nature Catalysis* thanks Yuanyue Liu, Edmund Dickinson and the other, anonymous, reviewer(s) for their contribution to the peer review of this work.

Reprints and permissions information is available at www.nature.com/reprints.

Publisher's note Springer Nature remains neutral with regard to jurisdictional claims in published maps and institutional affiliations.